

A spatial-correlation analysis of the cubic 3-torus topology based on the Planck 2013 data

R. Aurich

*Institut für Theoretische Physik, Universität Ulm,
Albert-Einstein-Allee 11,
D-89069 Ulm, Germany*

ABSTRACT

Spatial correlations of the cubic 3-torus topology are analysed using the Planck 2013 data. The spatial-correlation method for detecting multiply connected spaces is based on the fact that positions on the cosmic microwave background (CMB) sky, that are separated by large angular distances, can be spatially much nearer according to a hypothesized topology. The comparison of the correlations computed with and without the assumed topology can reveal whether a promising topological candidate is found. The level of the expected correlations is estimated by CMB simulations of the cubic 3-torus topology and compared to those obtained from the Planck data. An interesting 3-torus configuration is discovered which possesses topological correlations of the magnitude found in the CMB simulations based on a toroidal universe. Although the spatial-correlation method has a high false-positive rate, it is striking that there exists an orientation of a cubic 3-torus cell, where correlations between points that are separated by large angular distances, mimic those of closely separated points.

Key words: Cosmology: cosmic microwave background, large-scale structure of Universe

1 INTRODUCTION

The cosmic microwave background (CMB) radiation is of utmost importance to constrain the parameters of the cosmological concordance model, the Λ CDM model, because it reveals the state of the cosmos at a very early moment in its evolution. But its importance is not only due to this early snap-shot, since it also contains information of the cosmos on its largest scales. Therefore, the CMB radiation might also reveal the topology of the Universe, that is whether the space is simply connected or multiply connected. Apart from general considerations, the topic of cosmic topology (Lachièze-Rey and Luminet 1995; Luminet and Roukema 1999; Levin 2002; Rebouças and Gomero 2004; Mota et al. 2010, 2011; Fujii and Yoshii 2011) experiences a boost after the discovery of very low temperature correlations in the CMB by Hinshaw et al. (1996). This property is present in all subsequent CMB observations, see Copi et al. (2009, 2015) for a comparison of different data sets. The low temperature correlations are most obviously seen in the temperature two-point angular correlation function

$$C(\vartheta) := \langle \delta T(\hat{n}) \delta T(\hat{n}') \rangle \quad \text{with} \quad \hat{n} \cdot \hat{n}' = \cos \vartheta \quad , \quad (1)$$

where ϑ is the angular distance between the two directions \hat{n} and \hat{n}' on the surface of last scattering. The brackets denote averaging over the pixel pairs with $\hat{n} \cdot \hat{n}' = \cos \vartheta$. However, the central quantity in this paper is not the angular correla-

tion (1), but the spatial-correlation function $\xi(r)$, where r is the spatial distance between the two positions \hat{n} and \hat{n}' on the surface of last scattering. The spatial-correlation function $\xi(r)$ can be used as a tool for discovering a non-trivial topology of the Universe as suggested by Roukema et al. (2008). The idea is that the distance between two points q_1 and q_2 is not uniquely defined in a multiply connected space. On the one hand, one can compute the distance by completely ignoring the topology which means that one calculates the distance $d(q_1, q_2)$ in the universal cover. This leads to the definition of the correlation function

$$\xi_{\text{triv}}(r) := \frac{1}{C(0)} \langle \delta T(q_1) \delta T(q_2) \rangle \quad \text{with} \quad r = d(q_1, q_2) \quad , \quad (2)$$

where $C(0)$ normalizes the spatial correlation $\xi_{\text{triv}}(0) = 1$. On the other hand, one can use the shortest possible distance between q_1 and q_2 according to the assumed topological structure. This minimal distance might be computed by

$$d_{\Gamma}(q_1, q_2) := \min_{\gamma \in \Gamma} d(q_1, \gamma(q_2)) \quad , \quad (3)$$

where Γ denotes the covering group which defines the topology. However, for reasons that will become clear shortly, the topological test uses the slightly modified distance

$$d_{\text{topo}}(q_1, q_2) := \min_{\gamma \in \Gamma'} d(q_1, \gamma(q_2)) \quad , \quad (4)$$

where the $\Gamma' := \Gamma \setminus \{\text{id}\}$ is the set of group elements of Γ without the identity. For distances $d(q_1, q_2)$ smaller than the injectivity radius (Gomero and Rebouças 2003), one has $d_{\text{topo}}(q_1, q_2) > d(q_1, q_2)$, since the identity is removed. Removing the identity eliminates the distance $d(q_1, q_2)$ measured in the trivial topology, i.e. along the direct path in the universal cover, from the set of distances over which the minimum is taken in $d_{\text{topo}}(q_1, q_2)$. Therefore, small distances $d_{\text{topo}}(q_1, q_2)$ belong to widely separated points q_1 and q_2 on the sky that are located in different “copies” of the fundamental cell. If $d_{\text{topo}}(q_1, q_2)$ is computed for the correct topology, the distances $d_{\text{topo}}(q_1, q_2)$ and $d(q_1, q_2)$ provide two values of the distance between points q_1 and q_2 measured along different paths. Now, Roukema et al. (2008) define the topological correlation function

$$\xi_{\text{topo}}(r) := \frac{1}{C(0)} \langle \delta T(q_1) \delta T(q_2) \rangle \text{ with } r = d_{\text{topo}}(q_1, q_2), \quad (5)$$

which should reproduce $\xi_{\text{triv}}(r)$ under idealized conditions although the two functions are computed from different products $\delta T(q_1) \delta T(q_2)$. At scales r smaller than the injectivity radius, $\xi_{\text{triv}}(r)$ measures the correlations within the same fundamental cell, while $\xi_{\text{topo}}(r)$ measures them between different “copies” of the fundamental cell. Thus the small-scale behaviour $\xi_{\text{triv}}(r)$ should match $\xi_{\text{topo}}(r)$ even though the latter is obtained from widely separated pixels for small values of r as long as Γ belongs to the correct topology. Therefore, the aim of the method is to find a representation of Γ such that $\xi_{\text{topo}}(r)$ agrees with $\xi_{\text{triv}}(r)$ as far as possible.

It should be mentioned that in the case of a positive signal, the topology belonging to Γ might be confused with a different topology belonging to $\tilde{\Gamma}$, if Γ is a subgroup of $\tilde{\Gamma}$ that is $\Gamma \subset \tilde{\Gamma}$. In that case the minimum in equation (4) would be taken only over a subset. In the case of the 3-torus topology, this would mean that the “true” fundamental cell would tessellate the one found by the spatial-correlation method. Since smaller fundamental cells are easier to detect, this is unlikely to be the case.

It is worthwhile to note the relation to the matched circle test proposed by Cornish et al. (1998). The positions on a matched circle pair can be mapped onto each other by a group element $\gamma \in \Gamma'$. So the distance is $d_{\text{topo}}(q_1, q_2) = 0$ in this case. For zero distance $r = 0$, $\xi_{\text{topo}}(0)$ would thus measure the correlations between matched circle pairs on the CMB sky. In this way, $\xi_{\text{topo}}(0)$ gives an average of the correlations over all matched circle pairs.

Roukema et al. (2008) apply their spatial-correlation method to the Poincaré dodecahedral topology which is realized in a space with positive curvature. They investigate the three-year data of the Wilkinson Microwave Anisotropy Probe (WMAP) and find an interesting solution for a special orientation of the Poincaré dodecahedral cell. The same method is used by Aurich (2008) with respect to the cubic 3-torus topology which is the simplest non-trivial topology in flat space. The analysis based on the WMAP five-year data leads to a specific configuration of the cubic 3-torus topology where the spatial correlation $\xi_{\text{topo}}(r)$ is enhanced. Roukema et al. (2014) suggest to search for topologically lensed galaxy pairs in deep red-shift surveys according to the favoured 3-torus configuration and simulate the prospects of detecting that topology. In addition, they show in their figure 1 a variant of the topological correlation

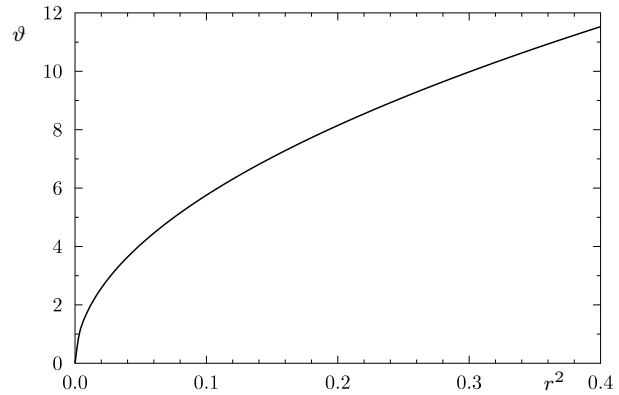


Figure 1. The projected angle ϑ onto the surface of last scattering is plotted in degrees as a function of the squared distance r^2 . The diameter $d_{\text{SLS}} = 6.2972$ of the surface of last scattering is used.

of the favoured orientation using the final WMAP nine-year data and demonstrate that also the latest WMAP data possess the spatial-correlation signature in favour of a 3-torus topology. In this paper the spatial-correlation analysis of the 3-torus topology is carried out for the Planck 2013 data (Planck Collaboration et al. 2014a) in order to see whether the signature persists.

In addition, in section 2 the spatial-correlation method is applied to simulated 3-torus CMB maps so that the correlations obtained from the Planck 2013 data can be compared to the expected signal. The analysis of the Planck data is the topic of section 3 and the final section 4 summarizes and discusses the results.

2 TEST OF THE SPATIAL-CORRELATION METHOD FOR THE 3-TORUS TOPOLOGY

The spatial-correlation method is tested for the cubic 3-torus topology. To that aim, torus CMB maps are computed for the Λ CDM model with the parameters given in Table 10 in Planck Collaboration et al. (2014a), column “Planck+WP+highL+BAO” with “Best fit”. The cosmological parameters are $\Omega_{\text{bar}} = 0.04825$, $\Omega_{\text{cdm}} = 0.2589$, $\Omega_{\Lambda} = 0.6928$, the reduced Hubble constant $h = 0.6777$, the reionisation optical depth $\tau = 0.0953$, and the scalar spectral index $n_s = 0.9611$. In the following, the side length L of the torus cell and the distance r are given in units of the Hubble length $L_H = c/H_0$. The distance to the surface of last scattering is $L_{\text{SLS}} = \Delta\eta L_H$ with $\Delta\eta = \eta_0 - \eta_{\text{rec}} = 3.1486$ and η being the conformal time. The diameter d_{SLS} of the surface of last scattering is $d_{\text{SLS}} = 2\Delta\eta = 6.2972$ in these units. It should be pointed out that this value is by a factor 0.95 smaller than the value obtained for a Λ CDM model favoured by the WMAP data where $\Delta\eta$ lies around 3.33. One has to bear this in mind when comparing length-scales from papers based on the WMAP concordance model. In the following, the spatial correlations will be analysed as functions of the squared distance r^2 , whose relation to the angle $\vartheta = 2\arcsin(r/d_{\text{SLS}})$ projected onto the surface of last scattering is plotted in figure 1. Most of the analyses consider the interval $r \in [0, r_{\text{max}}]$ with $r_{\text{max}}^2 = 0.4$ which translates to a projected angle of $\vartheta_{\text{max}} \simeq 11.5^\circ$.

The computation of $d_{\text{topo}}(q_1, q_2)$ requires the group Γ which has infinitely many elements in the case of the toroidal topology. The numerical analysis takes only the subset of Γ into account, which is obtained by concatenating at most four times the generators and their inverses. A larger subset would only be needed for very small fundamental cells.

With the above cosmological parameters, 100 CMB realisations of the cubic 3-torus topology with side length $L = 4$ are generated where 61 556 892 different eigenmodes are taken into account which belong to the first 50 000 eigenvalues. The spherical expansion of the eigenmodes is carried out up to $l_{\text{max}} = 1000$. In addition, 10 further torus simulations are computed which take only the usual Sachs-Wolfe contribution into account.

It is a common problem for all strategies, which try to detect a topological signature in the CMB sky, that only the usual Sachs-Wolfe contribution, which is proportional to the gravitational potential, would reveal a multiply connected space. Other contributions to the CMB sky do not possess this direct periodicity and thus reduce the expected topological signal. The two most important of them are the Doppler contribution and the integrated Sachs-Wolfe effect.

To demonstrate that difficulty and to test the general procedure, the spatial-correlation method is at first applied to the 10 CMB simulations that are based only on the usual Sachs-Wolfe contribution. The correlations are computed on sky maps which have a HEALPix resolution $N_{\text{side}} = 256$ and which are Gaussian smoothed with a width $\text{fwhm} = 24'$. Furthermore, the averaging in (2) and (5) is realized by sampling the products $\delta T(q_1) \delta T(q_2)$ in 40 equidistant intervals with respect to the variable r^2 up to $r^2 = 0.4$. The figure 2(a) shows for two such simulations the spatial-correlation functions $\xi_{\text{triv}}(r)$ (dotted curve) and $\xi_{\text{topo}}(r)$ (full curve). One observes that $\xi_{\text{topo}}(r)$ closely matches $\xi_{\text{triv}}(r)$ although the two are computed from completely different sets of products $\delta T(q_1) \delta T(q_2)$. The small deviations are due to the pixelisation and smoothing effects. In figure 2(b) the mean values obtained from the 10 functions $\xi_{\text{triv}}(r)$ and $\xi_{\text{topo}}(r)$ belonging to the 10 simulations are plotted as well as the 1σ band to indicate the width of the two distributions. The agreement between $\xi_{\text{triv}}(r)$ and $\xi_{\text{topo}}(r)$ is obtained only when the group Γ , which is used for the computation of $\xi_{\text{topo}}(r)$, is also the group for which the CMB simulation is computed. This is demonstrated for another torus configuration with side length $L = 4.41$, which will become important below. Applying the wrong group with respect to the torus simulations with $L = 4.0$ leads to correlations $\xi_{\text{topo}}(r)$ around zero, which are also shown in figure 2(b). This illustrates the principle of the spatial-correlation method under very idealized conditions.

The CMB radiation is, however, not only described by the usual Sachs-Wolfe contribution since a variety of physical effects modify it which destroys the idealized situation. Thus, 100 torus simulations are computed using a transfer function which takes the full Boltzmann physics into account. This includes the Doppler contribution, the integrated Sachs-Wolfe effect, Silk damping, reionisation, polarisation of photons and neutrinos assuming a standard thermal history. In this realistic scenario, the good agreement between $\xi_{\text{triv}}(r)$ and $\xi_{\text{topo}}(r)$, which is observed in figure 2, is lost. In figure 3(a) the spatial correlations $\xi_{\text{triv}}(r)$ and $\xi_{\text{topo}}(r)$ are plotted for such a realistic simulation. The cor-

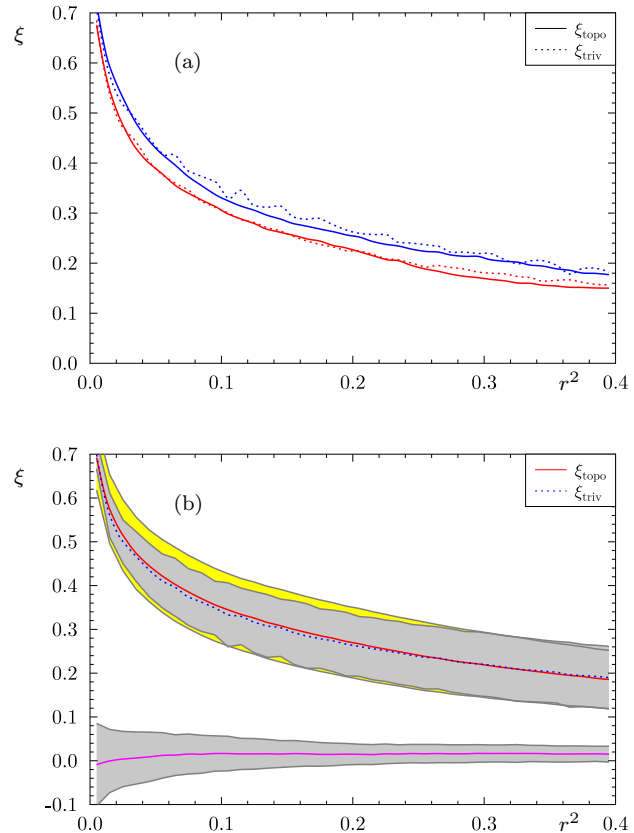


Figure 2. The spatial-correlation functions $\xi_{\text{triv}}(r)$ and $\xi_{\text{topo}}(r)$ are shown for the 3-torus topology based on CMB simulations which take only the usual Sachs-Wolfe contribution into account. The sky maps have a resolution of $N_{\text{side}} = 256$, and a Gaussian smoothing with $\text{fwhm} = 24'$ is applied. The Union mask U73 is used. In panel (a) the result from two simulations is plotted and the good agreement demonstrates the usability of the method. Panel (b) shows the distribution of the correlation functions for 10 simulations. The full curves for $\xi_{\text{topo}}(r)$ and the dotted curves for $\xi_{\text{triv}}(r)$ show the mean value whereas the bands show the 1σ width of the distributions. The lower band around zero belongs to correlations $\xi_{\text{topo}}(r)$ which are computed for a wrong configuration of the 3-torus cell. The upper two overlapping bands belong to $\xi_{\text{triv}}(r)$ (the smaller band) and to $\xi_{\text{topo}}(r)$ computed for the orientation used in the simulations.

relation $\xi_{\text{topo}}(r)$ is computed by using the same group Γ which is also used in the calculation of the torus sky map. The figure 3(a) reveals the extend to which the two correlation functions agree if the correct topology is used in $\xi_{\text{topo}}(r)$. Furthermore, a comparison between figures 2(a) and 3(a) shows that $\xi_{\text{triv}}(r)$ decreases with the inclusion of the full physics faster than without, although in both cases they are normalized by $\xi_{\text{triv}}(0) = 1$. Similar to figure 2(b), the figure 3(b) shows the average and the 1σ bands of the 100 torus simulations but now using the full transfer function. The three bands are, from top to bottom, the 1σ band for $\xi_{\text{triv}}(r)$, the 1σ band for $\xi_{\text{topo}}(r)$ using the correct configuration of the 3-torus cell, and the 1σ band for $\xi_{\text{topo}}(r)$ computed for a wrong configuration.

There is a further complication in the search for a topological signature in the spatial-correlation function. In the observed sky maps the dipole contribution is usually re-

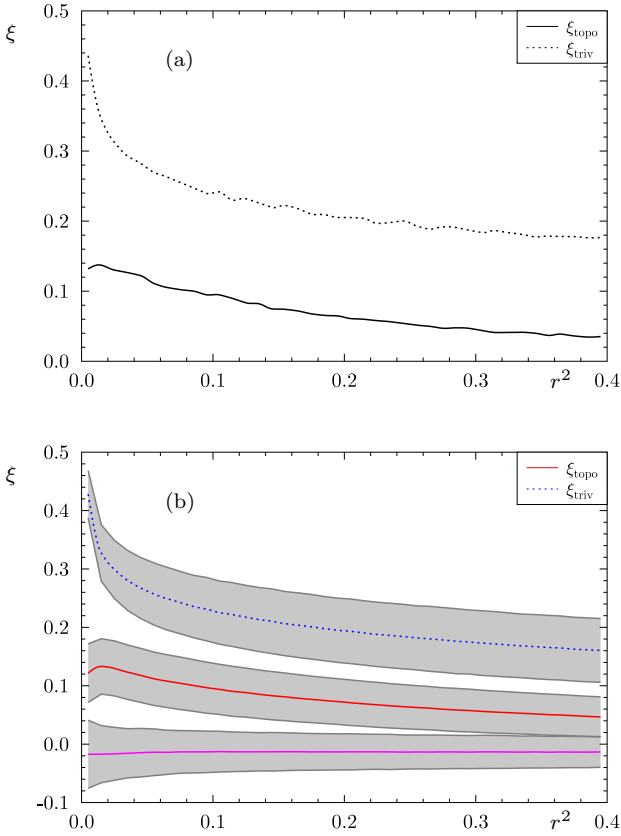


Figure 3. The spatial-correlation functions $\xi_{\text{triv}}(r)$ and $\xi_{\text{topo}}(r)$ are shown for the same 3-torus topology as in figure 2. However, in contrast to figure 2, the CMB simulations are now based on the full Boltzmann code taking the deteriorating effects into account. The resolution of the maps is again $N_{\text{side}} = 256$ and $\text{fwhm} = 24'$. The Union mask U73 is applied. Panel (a) reveals that the match between $\xi_{\text{triv}}(r)$ (dotted curve) and $\xi_{\text{topo}}(r)$ (full curve) is now much poorer than in figure 2(a) where only the usual Sachs-Wolfe contribution was considered, of course. Similar to figure 2(b), the panel (b) displays the distribution obtained from 100 3-torus simulations. The 1σ bands obtained from $\xi_{\text{triv}}(r)$ and from $\xi_{\text{topo}}(r)$ using the correct orientation no longer overlap. But the correlation $\xi_{\text{topo}}(r)$ is nevertheless significantly larger than those obtained from a wrong 3-torus orientation, as the lowest band around zero demonstrates.

moved because of the difficulty to separate the dynamic dipole due to our motion with respect to the CMB from the intrinsic dipole contribution (see e. g. Atrio-Barandela et al. (2014) and references therein). The 3-torus simulations do contain the intrinsic dipole. Therefore, in order to compare the Planck data with the simulations, one has to subtract the dipole in the simulations before computing the spatial-correlation functions. The change in the correlation functions is shown in figure 4, where the spatial-correlation functions are computed from the same 100 simulations as in figure 3(b) but now without the dipole contribution. The correlation $\xi_{\text{triv}}(r)$ decreases since a non-vanishing dipole leads to enhanced values in the correlation (2) for the considered small values of r belonging to two points q_1 and q_2 having a small angular separation. The reverse behaviour occurs for $\xi_{\text{topo}}(r)$, where small values of r belong to large angular separations where the dipole contribution has most likely a

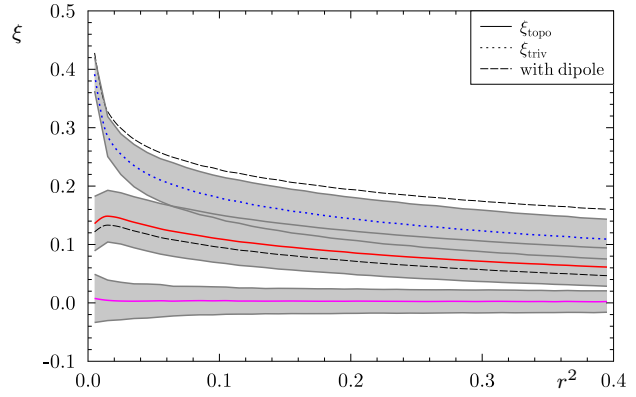


Figure 4. The spatial-correlation functions $\xi_{\text{triv}}(r)$ and $\xi_{\text{topo}}(r)$ are plotted for the same 3-torus simulations as in figure 3(b), but now the dipole contribution is set to zero. To guide the eye, the mean of $\xi_{\text{triv}}(r)$ and $\xi_{\text{topo}}(r)$ with the inclusion of the dipole are also shown as dashed curves. These are the same curves as in figure 3(b).

different sign at the two widely separated points q_1 and q_2 . This behaviour can be inferred from figure 4 where the mean correlations computed from sky maps with the dipole are also plotted (dashed curves). The 1σ bands obtained from the 100 simulations without the dipole contribution will be used below when the spatial correlations in the Planck data are analysed. In most cases, these are the 1σ bands of figure 4 where the resolution $\text{fwhm} = 24'$ is used. When CMB data are analysed in another resolution, the 1σ bands are computed from simulations with the corresponding resolution.

It might seem that the number of 100 CMB simulations is too small in order to extract the mean values and the 1σ bands belonging to the spatial-correlation functions of the 3-torus topology. In order to address this issue, figure 5 displays these curves obtained from the first 50 simulations from the set of the 100 simulations together with the results obtained from all 100 simulations. The mean values are nearly indistinguishable so that no significant alteration is expected for an even larger set of simulations. The 1σ boundaries show minute differences which indicate the accuracy that can be achieved from 100 simulations.

It is worthwhile to note that $\xi_{\text{topo}}(r)$, computed for the correct configuration, decreases at very small distances r as seen in figure 3(a). This tendency can also be seen for the average and the 1σ band in figures 3(b) and 4. This contrasts to $\xi_{\text{triv}}(r)$ which has its maximum at $r = 0$. Since this behaviour does not occur in figure 2 dealing with the pure usual Sachs-Wolfe contribution, it has to be ascribed to the deteriorating contributions contained in the full transfer function. Therefore, the degrading effects are less severe for slightly larger topological distances r . This shows that the spatial-correlation analysis can be a useful additional tool, since the matched circle test relies on $\xi_{\text{topo}}(r)$ at $r = 0$ as discussed in the introduction.

3 TOROIDAL CORRELATIONS IN THE PLANCK DATA

The correlation analysis of the torus simulations has the advantage that the underlying topology is known, of course.

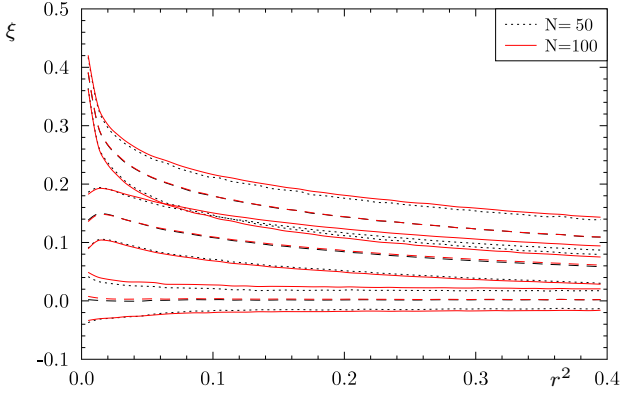


Figure 5. The mean values and the 1σ boundaries of the spatial-correlation functions $\xi_{\text{triv}}(r)$ and $\xi_{\text{topo}}(r)$ are plotted for the same 3-torus simulations as in figure 4. The dotted and full curves are based on the first 50 simulations and all 100 simulations, respectively. The figure shows that the mean values are almost unchanged while the slight differences in the 1σ boundaries reveal the order of the accuracy obtained from 100 simulations.

In the search for a spatial-correlation signature in the CMB data, a pseudo-probability estimator is required that measures the quality of the agreement between $\xi_{\text{triv}}(r)$ and $\xi_{\text{topo}}(r)$. Roukema et al. (2008) define this measure as

$$\mathcal{P} := \prod_{i=1}^n \begin{cases} e^{-\frac{(\xi_{\text{topo}}(i) - \xi_{\text{triv}}(i))^2}{2\sigma_i^2}} & \text{for } \xi_{\text{topo}}(i) \leq \xi_{\text{triv}}(i) \\ 1 + 0.01 \frac{\xi_{\text{topo}}(i) - \xi_{\text{triv}}(i)}{\xi_{\text{triv}}(i)} & \text{for } \xi_{\text{topo}}(i) \geq \xi_{\text{triv}}(i) \end{cases} \quad (6)$$

with

$$\sigma_i := \frac{1}{2} \xi_{\text{triv}}(i) \sqrt{\frac{N_n}{N_i}}. \quad (7)$$

Here, the index i runs over the bins for which the values of $\xi_{\text{topo}}(r)$ and $\xi_{\text{triv}}(r)$ are sampled. As described in section 2 the $r \in [0, r_{\text{max}}]$ interval is divided into $n = 40$ equidistant intervals with respect to the variable r^2 . The value $r_{\text{max}}^2 = 0.4$ is generally used with the exception of CMB maps having a large smoothing of $\text{fwhm} = 60'$, where $r_{\text{max}}^2 = 0.9$ is used, see below. The number of data points contributing to $\xi_{\text{triv}}(i)$ is denoted as N_i . The reason for choosing equidistant intervals with respect to r^2 is that for this binning the values of N_i are of the same order. This behaviour is revealed by figure 6 in the case of a map with $N_{\text{side}} = 256$ where the correlations are computed for every tenth pixel outside the Union mask U73 for a 3-torus topology with $L = 4$. In addition, figure 6 shows the number of pixels that contribute to the computation of $\xi_{\text{topo}}(i)$. Here, the minimum is obtained towards $r^2 = 0$, where $\xi_{\text{topo}}(i)$ gives an average over all matched circle pairs. This demonstrates that a lot of information is used by the spatial-correlation method beyond the matched circle pairs.

In the search for topological candidates, a modified probability is used in this paper. Using σ_i as defined in equation (7) leads to a weighting which disregards bins to which a small number N_i of data points contribute or bins with a large value of $\xi_{\text{triv}}(i)$. Thus, this weighting pays less attention to the pronounced peak in the correlation function at $r = 0$. The peak structure at $r = 0$ can be emphasized by modifying the probability

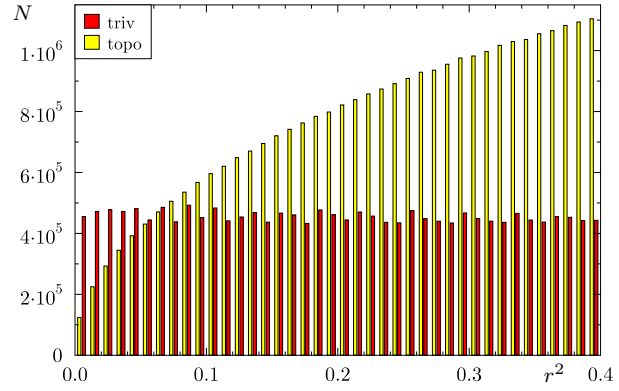


Figure 6. The number of pixel pairs are plotted that contribute to the computation of $\xi_{\text{triv}}(i)$ (red bins) and $\xi_{\text{topo}}(i)$ (yellow bins), where a 3-torus topology with $L = 4$ is tested. The numbers are obtained from a map with a resolution $N_{\text{side}} = 256$ outside the Union mask U73 and every tenth pixel is taken into account. The interval up to $r_{\text{max}}^2 = 0.4$ is divided into $n = 40$ bins.

$\ln \mathcal{P} = -\sum_{i=1}^n w_i \frac{(\xi_{\text{topo}}(i) - \xi_{\text{triv}}(i))^2}{2\sigma_i^2}$ with the weight $w_i := \xi_{\text{triv}}(i) / (\frac{1}{n} \sum_{j=1}^n \xi_{\text{triv}}(j))$. This leads to the weighting

$$\hat{\sigma}_i := \frac{1}{2} \sqrt{\xi_{\text{triv}}(i) \frac{1}{n} \sum_{j=1}^n \xi_{\text{triv}}(j)} \sqrt{\frac{N_n}{N_i}} \quad (8)$$

to be used in equation (6). This discussion shows that there is some arbitrariness in the choice of the pseudo-probability. It is clear that this choice determines to some degree which solution is considered as the optimal one as will be discussed below.

Using the probability (6) together with (7), Roukema et al. (2008) and Aurich (2008) used the Markov chain Monte Carlo (MCMC) method to search in the WMAP sky maps for a topological signal in favour of the Poincaré dodecahedral topology and of the cubic 3-torus topology, respectively. This paper addresses the question whether the cubic 3-torus candidate found by Aurich (2008) leads to an enhanced correlation $\xi_{\text{topo}}(r)$ also for the newer CMB data. The side length of the torus candidate was given as $L \simeq 3.84$ based on the concordance parameters given by WMAP. As discussed in section 2, this corresponds to $L \simeq 3.66$ using the concordance parameters given by Planck. The main effect from this shift arises from the lower Hubble constant H_0 . The ratio $L/d_{\text{SLS}} \simeq 0.58$ with respect to the diameter of the surface of last scattering is thus the same in both cases.

In figure 7(a) the spatial correlations $\xi_{\text{triv}}(r)$ and $\xi_{\text{topo}}(r)$ are plotted for the cubic 3-torus candidate with $L = 3.66$ and the orientation given by Aurich (2008) based on the WMAP five-year data (Gold et al. 2009). The figure 7(a) reveals that the WMAP five-year and the WMAP nine-year data (Bennett et al. 2013) lead to almost the same correlations. Here, the ILC maps outside the kq75 mask are used which have a resolution of $\text{fwhm} = 60'$. In order to compare these correlations with the Planck 2013 data, the SMICA map is smoothed to $\text{fwhm} = 60'$, and the correlations are computed outside the Union U73 mask (Planck Collaboration et al. 2014a). The topological correlation $\xi_{\text{topo}}(r)$ is almost indistinguishable from the WMAP

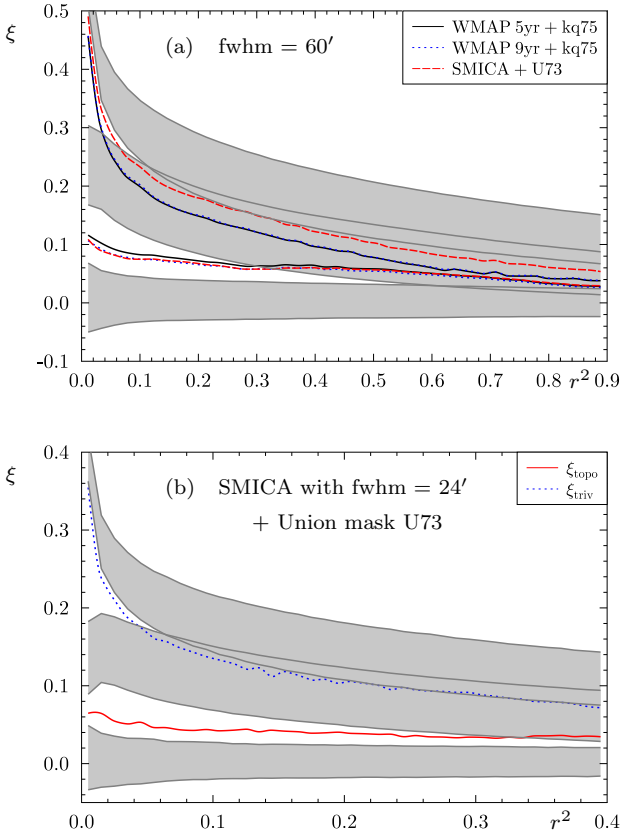


Figure 7. The correlation $\xi_{\text{topo}}(r)$ belonging to the $L = 3.66$ torus candidate is shown computed from different data sets. In panel (a), the correlations obtained from the WMAP five-year data (full curves) and the WMAP nine-year data (dotted curves) outside the kq75 mask are plotted together with correlations of the SMICA map outside the Union mask U73. The SMICA map is smoothed to the ILC resolution of $60'$. A pixelisation of $N_{\text{side}} = 256$ is used in all cases. The panel (b) displays the correlations for the higher resolution of $\text{fwhm} = 24'$ that is possible in the case of the SMICA map. Both figures show the 1σ bands computed from the 3-torus simulations with a resolution of $\text{fwhm} = 60'$ in panel (a) and with a resolution of $\text{fwhm} = 24'$ in panel (b).

nine-year result, but the correlation $\xi_{\text{triv}}(r)$ lies above the corresponding WMAP curves. Note, that $\xi_{\text{triv}}(r)$ is independent of any assumed topology, of course, and that this shift is, therefore, due to fine structures in the CMB maps. This effect also occurs in the angular correlation function $C(\vartheta)$, equation (1), which has different amplitudes at $\vartheta = 0^\circ$ for the WMAP and Planck data. Figure 7(a) also shows the 1σ bands obtained from the 3-torus simulations as described in section 2. It is seen that $\xi_{\text{topo}}(r)$ lies for $r^2 \gtrsim 0.35$ within the corresponding 1σ band, but drops below it for $r^2 \lesssim 0.35$. It is, however, above the 1σ band computed for the wrong torus configuration and, thus, remains an interesting candidate.

The correlation $\xi_{\text{triv}}(r)$ lies below the 1σ band of $\xi_{\text{triv}}(r)$ obtained from the torus simulations, but the deviation from the lower boundary of the 1σ band is much smaller for the Planck curve than for the WMAP curves, see figure 7(a). This lack of correlations at small distances should not be confused with the famous lack of correlations at large angles $\vartheta \gtrsim 60^\circ$ in $C(\vartheta)$, equation (1). The lack of correlations at

small distances in $\xi_{\text{triv}}(r)$ is also present in $C(\vartheta)$ at small angles. Non-trivial topological models are not only able to explain the lack of correlations at large angles, but also at small angles as shown by Aurich et al. (2005a) for the Poincaré dodecahedron and by Aurich et al. (2005b) for the Picard topology. The lack of correlations below $\vartheta < 30^\circ$ is investigated by Kim and Naselsky (2011) using the WMAP seven-year data and is found to be statistically significant. The analysis of the Planck Collaboration et al. (2014b) points to a less severe deviation which is consistent with figure 7(a). Since this anomaly or deviation does not concern $\xi_{\text{topo}}(r)$, it is considered hereafter as an observational fact.

Since the SMICA map possesses a resolution of $\text{fwhm} = 5'$, it is interesting to see how a better resolution influences the correlations. In the following figures concerning the spatial-correlation functions, the distance r is restricted to $r^2 \leq 0.4$ in order to emphasize the peak structure. For this smaller interval, figure 7(b) displays the correlations computed from the SMICA map where a Gaussian smoothing with $\text{fwhm} = 24'$ is applied and which is downgraded to $N_{\text{side}} = 256$. Furthermore, only pixels outside the Union mask U73 are taken into account. The correlation $\xi_{\text{topo}}(r)$ lies for $r^2 \lesssim 0.3$ below the 1σ band computed for the correct torus configuration, but well above the 1σ band belonging to the wrong configuration. The correlation $\xi_{\text{triv}}(r)$ lies slightly below the corresponding 1σ band, as it is the case for the lower resolution shown in panel (a). So the conclusion is that this 3-torus configuration is interesting because it leads to an enhanced topological correlation $\xi_{\text{topo}}(r)$.

The SMICA map with the resolution $\text{fwhm} = 24'$ and $N_{\text{side}} = 256$ is also used to search for further interesting configurations by applying the MCMC method. Only pixels outside the Union mask U73 are taken into account. The parameter space consists of the side length L and the three Euler angles defining the orientation of the cubic 3-torus cell. A random point in this four-dimensional parameter space is selected as the starting point for the MCMC algorithm which generates a sequence of points with the aim to find more likely configurations according to the pseudo-probability (6). This method works fine when the region with the enhanced probability is not too localized, since otherwise the Markov chain can miss the interesting domain. Thus, an alternative program without using the MCMC algorithm is carried out which does a simple random search. A large set of $N = 2\,000\,000$ random points is generated from the parameter space and the corresponding pseudo-probabilities (6) using $\hat{\sigma}_i$, equation (8), are computed in order to find interesting configurations. The distance interval is again chosen as $r^2 \in [0, 0.4]$. The parameter space of the random search is confined to $L \in [3.5, 5.5]$, but the three Euler angles are generated without restrictions. This random search discovers a cubic 3-torus configuration with a much better agreement with the expected topological signature. After the random search has found a new more interesting 3-torus candidate, a MCMC chain is generated, which uses as the starting point the parameters of this new candidate. This MCMC chain of length 100 000 explores the parameter space around the candidate and reveals the generators of the group Γ for a sample of 3-torus configurations with large correlations $\xi_{\text{topo}}(r)$.

The new candidate has a side-length $L \simeq 4.41$, i.e. $L/d_{\text{SLS}} \simeq 0.70$, and the spatial correlations are shown in figures 8 and 9. Figure 8(a) displays the correlations computed

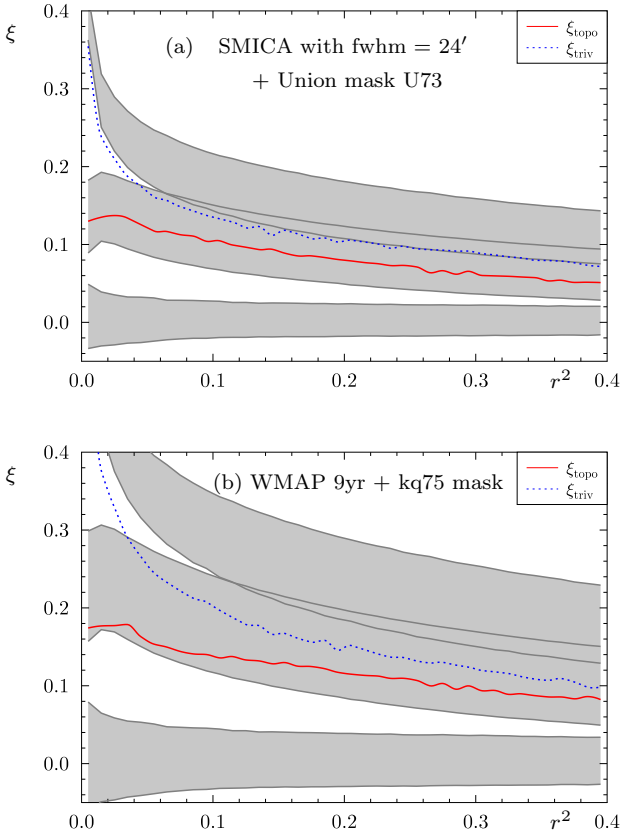


Figure 8. The correlation $\xi_{\text{topo}}(r)$ is computed for the 3-torus candidate with side length $L = 4.41$ and the orientation given in the text. The spatial correlations obtained from the SMICA map using the Union mask U73 are plotted in panel (a) and from the WMAP 9yr ILC map using the kq75 mask in panel (b). The resolution of the maps is again $N_{\text{side}} = 256$, and the Planck map is smoothed with $\text{fwhm} = 24'$. No smoothing is applied to the ILC map because of its lower resolution of $60'$. The 1σ bands of figure 4 are shown in panel (a). In panel (b), the 1σ bands for the lower resolution are plotted. It is striking to observe in panel (a) that $\xi_{\text{topo}}(r)$ obtained from the Planck data almost agrees with the mean topological correlation derived from the 3-torus simulations for a correct identification. On the other hand, $\xi_{\text{triv}}(r)$ lies below the corresponding 1σ band of the simulations. However, this implies that the match between $\xi_{\text{topo}}(r)$ and $\xi_{\text{triv}}(r)$ is even better than in many simulations. The good agreement between $\xi_{\text{topo}}(r)$ and $\xi_{\text{triv}}(r)$ is also present in the WMAP 9yr data as panel (b) reveals using a resolution of $\text{fwhm} = 60'$.

from the SMICA map with the resolution $\text{fwhm} = 24'$ and $N_{\text{side}} = 256$ outside the Union mask U73. The correlation $\xi_{\text{triv}}(r)$ is the same as in figure 7(b) since both figures refer to the same CMB map. The topological correlation $\xi_{\text{topo}}(r)$ of the $L = 4.41$ candidate is very close to the mean of the correlations obtained from the torus simulations when the correct orientation is used. The comparison of figure 7(b) with 8(a) reveals the improvement with respect to the topological signal of the $L = 4.41$ candidate. It is striking to see the agreement between $\xi_{\text{topo}}(r)$ and $\xi_{\text{triv}}(r)$ in figure 8(a).

To answer the question whether this candidate is also distinguished in the WMAP data, figure 8(b) shows the correlations computed from the WMAP nine-year ILC map outside the kq75 mask. The ILC map has a resolution of

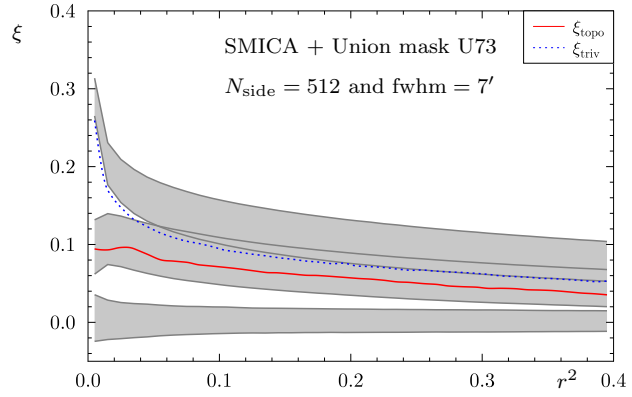


Figure 9. As in figure 8(a) the spatial-correlation functions $\xi_{\text{triv}}(r)$ and $\xi_{\text{topo}}(r)$ obtained from the SMICA map using the Union mask U73 are plotted, but now the resolutions of all maps are $N_{\text{side}} = 512$ and $\text{fwhm} = 7'$. The result is very similar to that shown in figure 8(a), only the amplitudes are reduced overall.

l	13°	42°	123°	193°	222°	303°
b	-55°	31°	-14°	55°	-31°	14°

Table 1. The positions of the fundamental symmetry axes of the cubic 3-torus candidate are listed in Galactic coordinates (l, b) . The values are rounded to one degree.

$\text{fwhm} = 60'$ and the corresponding 1σ bands are shown. As in the case of the Planck data, the agreement between $\xi_{\text{triv}}(r)$ and $\xi_{\text{topo}}(r)$ is quite well. This candidate thus might have been discovered by Aurich (2008), but the Markov chains overlooked this interesting domain in the four-dimensional parameter space and thus failed to notice this torus configuration. This demonstrates that searches for topological spaces with more than four parameters would have to be treated with even more care.

The SMICA map possesses a resolution of $\text{fwhm} = 5'$. This map is Gaussian smoothed with $\text{fwhm} = 5'$ leading to a map with an effective resolution of $\text{fwhm} = 7'$. This map is downgraded to $N_{\text{side}} = 512$ and the corresponding spatial correlations are plotted in figure 9 together with the appropriate 1σ bands. It is seen that the topological correlation $\xi_{\text{topo}}(r)$ is close to $\xi_{\text{triv}}(r)$ also in this higher resolution.

The large values in the correlation $\xi_{\text{topo}}(r)$ might be accidentally generated by the structure of the mask for the special torus configuration with $L \simeq 4.41$. To provide evidence that this is unlikely, the 3-torus simulations computed for $L = 4.00$ are used to compute the correlations for the configuration of the $L = 4.41$ candidate. Since this is not the configuration used in the CMB simulations, one obtains the 1σ band for the wrong configuration shown in the previous figures, i. e. the 1σ the band around zero. This disproves the possibility of a spurious correlation somehow generated by the structure of the mask.

The MCMC chain, which explores the parameter space around the $L = 4.41$ candidate, can be used to reveal the orientation of the cubic 3-torus cell. The three generators of Γ define three axes through our observer position, which intersect the surface of last scattering at six positions. The positions of these fundamental directions are shown in figure

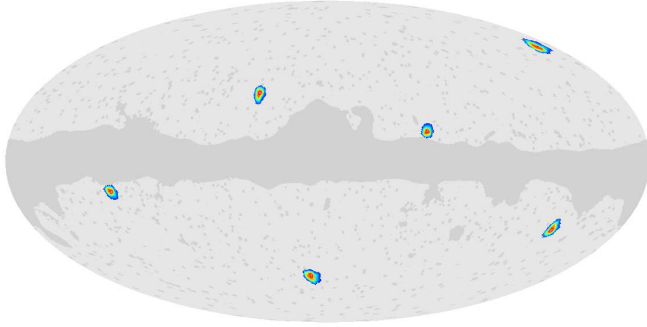


Figure 10. The orientation of the fundamental symmetry axes of the cubic 3-torus candidate around $L = 4.41$ are shown using the Mollweide projection. Galactic coordinates are used and the Galactic centre lies in the centre of the plot. The Union mask U73 is also indicated by the shaded region.

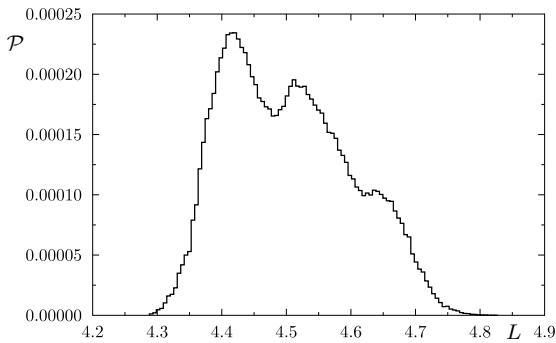


Figure 11. The largest values of \mathcal{P} using $\hat{\sigma}_i$ as defined in equation (8) are plotted as a function of L . The maximum of \mathcal{P} is computed over all orientations within a small L interval.

10, where the full sky is mapped by the Mollweide projection using Galactic coordinates. The intensities are plotted according to \mathcal{P} using $\hat{\sigma}_i$ as defined in equation (8), which is also used for the computation of the MCMC chain. The positions of the six fundamental directions are given in table 1.

The configurations generated by the MCMC algorithm contain not only the three Euler angles, but also the side length L of the cubic 3-torus cell. The L values are now grouped into bins and within each bin, the maximal value of \mathcal{P} is searched regardless of the orientations of the cells. The resulting curve, shown in figure 11, displays a bimodal distribution. The largest value of \mathcal{P} belongs to the $L = 4.41$ candidate discussed above. The second maximum occurs at $L = 4.52$ but the orientation is nearly identical. The fact that the orientations are very similar, can be inferred from figure 10, where the \mathcal{P} values of all members of the MCMC chain are taken into account. Another orientation would lead to a plot with further six directions with high probabilities, but this is not the case. The correlations $\xi_{\text{topo}}(r)$ belonging to the two models with $L = 4.41$ and $L = 4.52$ are compared in figure 12. For $r^2 \gtrsim 0.08$ the topological correlation is even larger for the $L = 4.52$ model than for the $L = 4.41$ configuration, but at small values of r^2 the cor-

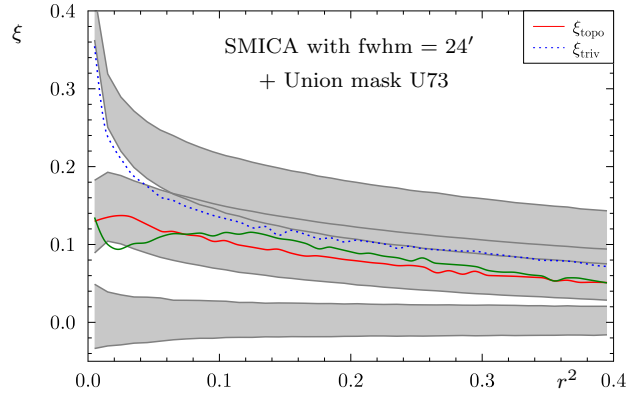


Figure 12. The correlation $\xi_{\text{topo}}(r)$ is shown for the $L = 4.41$ candidate as in figure 8(a), but, in addition, the correlation of the $L = 4.52$ configuration is also plotted which belongs to the second maximum shown in figure 11. The latter correlation is enhanced for $r^2 \gtrsim 0.08$, but is reduced for smaller values of r^2 compared to $\xi_{\text{topo}}(r)$ belonging to the $L = 4.41$ candidate.

relation is reduced. Since the chosen pseudo-probability \mathcal{P} tries to emphasize the peak structure at $r = 0$ in $\xi_{\text{triv}}(r)$, as discussed at the beginning of section 3, the model with $L = 4.41$ is slightly preferred. Although other versions of \mathcal{P} would favour other models, the general conclusion would be unchanged that the orientation given in table 1 leads to large correlations $\xi_{\text{topo}}(r)$ with $r^2 \leq 0.4$ for values of L in the range shown in figure 11. Furthermore, the topological correlation $\xi_{\text{topo}}(r)$ matches the expectation derived from the 100 CMB simulations of the cubic 3-torus topology.

Although the analysis of this paper is based on the Planck 2013 data, it is interesting to see whether the recently published Planck 2015 data (Planck Collaboration et al. 2015) also display the enhanced spatial correlations for the $L = 4.41$ candidate. The temperature differences outside the masks between the 2013 and 2015 data sets are stated to be of the order of at most $\sim 10 \mu K$ by Planck Collaboration et al. (2015). Thus, only modest differences are expected, and this is confirmed by figure 13, where $\xi_{\text{topo}}(r)$ is plotted for the $L = 4.41$ candidate using the 2013 SMICA map as above, as well as using the recently published 2015 SMICA map. The corresponding curves of $\xi_{\text{topo}}(r)$ and $\xi_{\text{triv}}(r)$ are each nearly indistinguishable. A MCMC chain of length 100 000 is generated which explores the parameter space around the $L = 4.41$ candidate based on the 2015 data. The orientation of the fundamental symmetry axes of the cubic 3-torus candidate turns out as depicted in figure 10 which is obtained from the 2013 data. The axes obtained from the 2015 data agree with those given in table 1.

4 SUMMARY AND DISCUSSION

Roukema et al. (2008) put forward the idea that a spatial-correlation analysis can serve as a tool for detecting the topology of our Universe. The topological correlation $\xi_{\text{topo}}(r)$, defined in equation (5), should agree with the correlation $\xi_{\text{triv}}(r)$, equation (2), if the hypothesized topology used for the computation of $\xi_{\text{topo}}(r)$ matches the true topology.

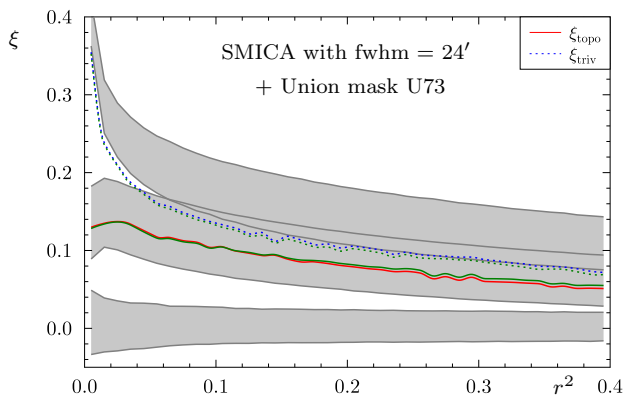


Figure 13. The correlations $\xi_{\text{topo}}(r)$ and $\xi_{\text{triv}}(r)$ are shown for the $L = 4.41$ candidate as in figure 8(a). In addition, the correlations $\xi_{\text{topo}}(r)$ and $\xi_{\text{triv}}(r)$ are plotted that are obtained from the Planck 2015 data using the Union mask U73. Both correlations are almost identical to those obtained from the 2013 data, although the 2015 correlation $\xi_{\text{topo}}(r)$ is slightly enhanced for $r^2 \gtrsim 0.2$.

The spatial-correlation analysis is applied to the cubic 3-torus topology using the Planck 2013 data. CMB simulations for the cubic 3-torus topology are generated and analysed with respect to the spatial correlation in section 2. This allows to estimate the level of correlations that is to be expected if a suitable configuration is found. It is shown that the agreement between $\xi_{\text{topo}}(r)$ and $\xi_{\text{triv}}(r)$ is very good only under very idealized conditions where the CMB simulations take only the usual Sachs-Wolfe contribution into account. Although a realistic CMB simulation based on the Boltzmann physics leads to enhanced topological correlations $\xi_{\text{topo}}(r)$, they nevertheless lie appreciably below $\xi_{\text{triv}}(r)$ as shown in figure 4.

The cubic 3-torus configuration which was found by Aurich (2008) as having a large topological correlation $\xi_{\text{topo}}(r)$ using the WMAP five-year data, is reanalysed in section 3 using the Planck 2013 data. Figure 7 shows that the topological correlation is indeed of the expected magnitude for not too small distances r , but possesses relatively small values of $\xi_{\text{topo}}(r)$ for small distances and does not match the increasing behaviour found in CMB 3-torus simulations. An improved search for configurations of the cubic 3-torus topology found, however, a new candidate, which has a topological correlation $\xi_{\text{topo}}(r)$ that is very close to the mean topological correlation obtained from 100 torus simulations. This configuration is denoted as the $L = 4.41$ candidate and its correlation is shown in figures 8, 9, and 13. The orientation of its fundamental symmetry axes is visualized in figure 10 and listed in table 1.

Although the agreement with the expected correlation is amazing, one must keep in mind that the spatial-correlation method has a relative high false-positive rate. To determine this rate, it is necessary to carry out the search for a matching topology with CMB simulations generated for the trivial topology. This demanding computation is done by Aurich (2008) for 10 such CMB simulations, and it turns out that one of these 10 simulations generates a high correlation by chance. Based on this limited number of simulations, a false-positive rate of the order of one to ten is expected, and Aurich (2008) concludes that $\sim 10\% \dots 20\%$ of the simula-

tions would produce such a false-positive detection. It should be noted that these simulations are carried out in the lower HEALPix resolution $N_{\text{side}} = 128$ in contrast to this paper, where the higher resolution $N_{\text{side}} = 256$ or even $N_{\text{side}} = 512$ is used. Nevertheless, the order of the false-positive detection rate should carry over to the resolution used in this paper, since the resolution does not significantly change the spatial correlations as the comparison of figure 8(a) with figure 9 shows. The former is computed for $N_{\text{side}} = 256$ and $\text{fwhm} = 24'$ and the latter for $N_{\text{side}} = 512$ and $\text{fwhm} = 7'$, and a very similar result is obtained. In addition, figures 7(a) and 7(b) allow a comparison between the resolutions $\text{fwhm} = 60'$ and $\text{fwhm} = 24'$ again with very similar spatial correlations. Therefore, the false-positive rate is of the order of one to ten.

Furthermore, the Planck 2013 data are analysed with respect to a non-trivial topology by the Planck Collaboration et al. (2014c) and no convincing signal is detected by the matched circle test and by using off-diagonal correlations. The application of the covariance matrix for detecting a toroidal universe is discussed by Kunz et al. (2006, 2008); Phillips and Kogut (2006). It should be noted that the use of the covariance matrix $C_{lm}^{l'm'} := \langle a_{lm} a_{l'm'}^* \rangle$ can fail to detect a topology if the phases of a_{lm} are not accurately enough determined as shown by Aurich et al. (2008) where the influence of a mask is investigated. Nevertheless, it remains the point that no hints in favour of a toroidal universe come from the matched circle test and from off-diagonal correlations.

This points to a false-positive detection. However, it might be that the simulations underestimate the deteriorating effects, which disturb the CMB with respect to the clean signal that would be obtained from the usual Sachs-Wolfe contribution. A hint in this direction is the fact that the cross-correlation of the CMB radiation with the large-scale galaxy distribution is significantly stronger than expected (Granett et al. 2008; Aiola et al. 2015). This points to the possibility that the late-time integrated Sachs-Wolfe effect is larger than predicted by the Λ CDM concordance model. The CMB simulations are based on the Λ CDM concordance model and thus do not include such currently inexplicable contributions. However, the Λ CDM model is used to discriminate between a spurious signal and a signal corresponding to a genuine detection of a non-trivial topology. This estimation of the detection level might be flawed due to additional correlations that do not have their origin at the surface of last scattering.

There remains the question whether the 3-torus topology is hidden in the CMB data. But even if the enhanced spatial correlation of the $L = 4.41$ candidate is not due to a cubic 3-torus topology, it is nevertheless striking that there exists an orientation of a torus cell, for which a large correlation in the CMB data is found.

ACKNOWLEDGEMENTS

HEALPix [healpix.jpl.nasa.gov] (Górski et al. 2005) and the Planck as well as WMAP data from the LAMBDA website (lambda.gsfc.nasa.gov) were used in this work.

REFERENCES

- Aiola, S., Kosowsky, A., and Wang, B. (2015). Gaussian Approximation of Peak Values in the Integrated Sachs-Wolfe Effect. *Phys. Rev. D*, 91(4):043510, arXiv:1410.6138 [astro-ph.CO].
- Atrio-Barandela, F., Kashlinsky, A., Ebeling, H., Fixsen, D. J., and Kocevski, D. (2014). Probing the Dark Flow signal in WMAP 9 yr and PLANCK cosmic microwave background maps. *ArXiv e-prints*, arXiv:1411.4180 [astro-ph.CO].
- Aurich, R. (2008). A spatial correlation analysis for a toroidal universe. *Class. Quantum Grav.*, 25:225017, arXiv:0803.2130 [astro-ph].
- Aurich, R., Janzer, H. S., Lustig, S., and Steiner, F. (2008). Do we Live in a "Small Universe"? *Class. Quantum Grav.*, 25:125006, arXiv:0708.1420 [astro-ph].
- Aurich, R., Lustig, S., and Steiner, F. (2005a). CMB anisotropy of the Poincaré Dodecahedron. *Class. Quantum Grav.*, 22:2061–2083, arXiv:astro-ph/0412569.
- Aurich, R., Lustig, S., Steiner, F., and Then, H. (2005b). Indications about the shape of the Universe from the Wilkinson Microwave Anisotropy Probe data. *Phys. Rev. Lett.*, 94:021301–1–4, arXiv:astro-ph/0412407.
- Bennett, C. L., Larson, D., Weiland, J. L., Jarosik, N., Hinshaw, G., Odegard, N., Smith, K. M., Hill, R. S., Gold, B., Halpern, M., Komatsu, E., Nolte, M. R., Page, L., Spergel, D. N., Wollack, E., Dunkley, J., Kogut, A., Limon, M., Meyer, S. S., Tucker, G. S., and Wright, E. L. (2013). Nine-Year Wilkinson Microwave Anisotropy Probe (WMAP) Observations: Final Maps and Results. *Astrophys. J. Supp.*, 208:20, arXiv:1212.5225 [astro-ph.CO].
- Copi, C. J., Huterer, D., Schwarz, D. J., and Starkman, G. D. (2009). No large-angle correlations on the non-Galactic microwave sky. *Mon. Not. R. Astron. Soc.*, 399:295–303, arXiv:0808.3767 [astro-ph].
- Copi, C. J., Huterer, D., Schwarz, D. J., and Starkman, G. D. (2015). Lack of large-angle TT correlations persists in WMAP and Planck. *Mon. Not. R. Astron. Soc.*, 451:2978–2985, arXiv:1310.3831 [astro-ph.CO].
- Cornish, N. J., Spergel, D. N., and Starkman, G. D. (1998). Circles in the sky: finding topology with the microwave background radiation. *Class. Quantum Grav.*, 15:2657–2670, arXiv:astro-ph/9801212.
- Fujii, H. and Yoshii, Y. (2011). An improved cosmic crystallography method to detect holonomies in flat spaces. *Astron. & Astrophys.*, 529:A121, arXiv:1103.1466 [astro-ph.CO].
- Gold, B., Bennett, C. L., Hill, R. S., Hinshaw, G., Odegard, N., Page, L., Spergel, D. N., Weiland, J. L., Dunkley, J., Halpern, M., Jarosik, N., Kogut, A., Komatsu, E., Larson, D., Meyer, S. S., Nolte, M. R., Wollack, E., and Wright, E. L. (2009). Five-Year Wilkinson Microwave Anisotropy Probe (WMAP) Observations: Galactic Foreground Emission. *Astrophys. J. Supp.*, 180:265–282, arXiv:0803.0715 [astro-ph].
- Gomero, G. I. and Rebouças, M. J. (2003). Detectability of cosmic topology in flat universes. *Physics Letters A*, 311:319–330, arXiv:gr-qc/0202094.
- Górski, K. M., Hivon, E., Banday, A. J., Wandelt, B. D., Hansen, F. K., Reinecke, M., and Bartelmann, M. (2005). HEALPix: A Framework for High-Resolution Discretization and Fast Analysis of Data Distributed on the Sphere. *Astrophys. J.*, 622:759–771. HEALPix web-site: <http://healpix.jpl.nasa.gov/>.
- Granett, B. R., Neyrinck, M. C., and Szapudi, I. (2008). An Imprint of Superstructures on the Microwave Background due to the Integrated Sachs-Wolfe Effect. *Astrophys. J. Lett.*, 683:L99–L102, arXiv:0805.3695 [astro-ph].
- Hinshaw, G., Banday, A. J., Bennett, C. L., Górski, K. M., Kogut, A., Lineweaver, C. H., Smoot, G. F., and Wright, E. L. (1996). Two-Point Correlations in the COBE DMR Four-Year Anisotropy Maps. *Astrophys. J. Lett.*, 464:L25–L28.
- Kim, J. and Naselsky, P. (2011). Lack of Angular Correlation and Odd-parity Preference in Cosmic Microwave Background Data. *Astrophys. J.*, 739:79, arXiv:1011.0377 [astro-ph.CO].
- Kunz, M., Aghanim, N., Cayon, L., Forni, O., Riazuelo, A., and Uzan, J. P. (2006). Constraining topology in harmonic space. *Phys. Rev. D*, 73(2):023511–+, arXiv:astro-ph/0510164.
- Kunz, M., Aghanim, N., Riazuelo, A., and Forni, O. (2008). On the detectability of non-trivial topologies. *Phys. Rev. D*, 77:023525, arXiv:astro-ph/0704.3076.
- Lachièze-Rey, M. and Luminet, J.-P. (1995). Cosmic topology. *Physics Report*, 254:135–214.
- Levin, J. (2002). Topology and the cosmic microwave background. *Physics Report*, 365:251–333.
- Luminet, J.-P. and Roukema, B. F. (1999). Topology of the Universe: Theory and Observation. In *NATO ASIC Proc. 541: Theoretical and Observational Cosmology*, page 117. Kluwer, astro-ph/9901364.
- Mota, B., Rebouças, M. J., and Tavakol, R. (2010). Circles-in-the-sky searches and observable cosmic topology in a flat universe. *Phys. Rev. D*, 81:103516, arXiv:1002.0834 [astro-ph.CO].
- Mota, B., Rebouças, M. J., and Tavakol, R. (2011). What can the detection of a single pair of circles-in-the-sky tell us about the geometry and topology of the Universe? *Phys. Rev. D*, 84:083507, arXiv:1108.2842 [astro-ph.CO].
- Phillips, N. G. and Kogut, A. (2006). Constraints on the Topology of the Universe from the Wilkinson Microwave Anisotropy Probe First-Year Sky Maps. *Astrophys. J.*, 645:820–825, arXiv:astro-ph/0404400.
- Planck Collaboration, Adam, R., Ade, P. A. R., Aghanim, N., Arnaud, M., Ashdown, M., Aumont, J., Baccigalupi, C., Banday, A. J., Barreiro, R. B., and et al. (2015). Planck 2015 results. IX. Diffuse component separation: CMB maps. *ArXiv e-prints*, 1502.05956.
- Planck Collaboration, Ade, P. A. R., Aghanim, N., Alves, M. I. R., Armitage-Caplan, C., Arnaud, M., Ashdown, M., Atrio-Barandela, F., Aumont, J., Aussel, H., and et al. (2014a). Planck 2013 results. I. Overview of products and scientific results. *Astron. & Astrophys.*, 571:A1, arXiv:1303.5062.
- Planck Collaboration, Ade, P. A. R., Aghanim, N., Armitage-Caplan, C., Arnaud, M., Ashdown, M., Atrio-Barandela, F., Aumont, J., Baccigalupi, C., Banday, A. J., and et al. (2014b). Planck 2013 results. XXIII. Isotropy and statistics of the CMB. *Astron. & Astrophys.*, 571:A23, arXiv:1303.5083 [astro-ph.CO].
- Planck Collaboration, Ade, P. A. R., Aghanim, N.,

- Armitage-Caplan, C., Arnaud, M., Ashdown, M., Atrio-Barandela, F., Aumont, J., Baccigalupi, C., Banday, A. J., and et al. (2014c). Planck 2013 results. XXVI. Background geometry and topology of the Universe. *Astron. & Astrophys.*, 571:A26, arXiv:1303.5086 [astro-ph.CO].
- Rebouças, M. J. and Gomero, G. I. (2004). Cosmic Topology: a Brief Overview. *Braz. J. Phys.*, 34:1358–1366, arXiv:astro-ph/0402324.
- Roukema, B. F., Buliński, Z., Szaniewska, A., and Gaudin, N. E. (2008). The optimal phase of the generalised Poincare Dodecahedral Space hypothesis implied by the spatial cross-correlation function of the WMAP sky maps. *Astron. & Astrophys.*, 486:55, arXiv:0801.0006 [astro-ph].
- Roukema, B. F., France, M. J., Kazimierczak, T. A., and Buchert, T. (2014). Deep redshift topological lensing: strategies for the T^3 candidate. *Mon. Not. R. Astron. Soc.*, 437:1096–1108, arXiv:1302.4425 [astro-ph.CO].